Barbu, L.G., Martinez, X., Oller, S. and Barbat, A.H. Validation on large scale tests of a new hardening-softening law for the Barcelona plastic damage model, International Journal of Fatigue (2015); 81:213-226, doi:10.1016/j.ijfatigue.2015.07.031

Validation on large scale tests of a new hardening-softening law for the Barcelona plastic damage model

Lucia G. Barbu[a,b,*], Xavier Martinez[a,c], Sergio Oller[a,b] and Alex H. Barbat[a,b]

a. International Center for Numerical Methods in Engineering (CIMNE). Campus Nord, Gran Capità s/n, 08034 Barcelona, Spain
b. Department of Strenght of Materials and Structural Engineering - UPC. Edifici C1, Campus Nord, Jordi Girona 1-3, 08034 Barcelona, Spain
c. Department of Nautical Science and Engineering - UPC. Pla de Palau 18, 08003 Barcelona, Spain

[*] Corresponding author. Tel +34 934016473, e-mail: lgratiela@cimne.upc.edu

Abstract. This paper presents the results of finite element simulations made on a bent pipe subjected to an in-plane variable cyclic displacement combined with internal pressure. Special emphasis is put on the capacity of the model to illustrate different failure modes depending on the internal pressure applied on the pipe. The results of the numerical analyses will be compared to experimental ones. The constitutive model used for the simulation of Ultra Low Cycle Fatigue (ULCF) loading and the hardening–softening law used are only briefly touched upon. The monotonic behavior of a large diameter pipe, as obtained from the constitutive model proposed, is also shown and compared to experimental results under two different loading conditions. The total axial load at failure for this case resulted in less than 10% error as compared to the experiments. Regarding the ULCF in-plane bending simulations conducted on a 16-inch 90° elbow, the results were in good agreement with the experimental test in terms of force-displacement hysteresis loops and total fatigue life of the specimen. An analysis of the dependence of the failure mode to the internal pressure applied has been conducted, showing that the formulation is capable of obtaining both habitual failure types.

Keywords: Ultra Low Cycle Fatigue; Plastic damage; Isotropic hardening; Kinematic hardening; Constitutive modelling

1. Introduction

ULCF can occur in the metallic materials of modern steel devices that are designed to absorb seismic energy by sustaining large inelastic deformations under cyclic loads. Pipelines installed in seismic or permafrost regions must have sufficient strength against buckling or fracture caused by large ground deformation of buried pipeline.

ULCF can be defined as a failure that occurs at a relatively small number on the repeated stress or strain cycles. The upper limit in low-cycle life has generally been selected arbitrarily by different researchers to lie in the range of 10^4 to 10^5 cycles. On the other hand, the lower limit of life is the static test which has been represented by various investigators as 1/4, 1/2, 3/4 or even one cycle ([1], [2]). For ductile metals under periodic plastic loading, materials often fail within a reduced number of life cycles. Within this regime, the failure mechanism is governed by the plastic and damage (or sometimes called ductile damage), which is characterized by micro structure deterioration such as micro void nucleation, growth and coalescence and micro crack

initiation and propagation [3]. So, this process is governed by void growth and coalescence-type mechanisms, which are associated, typically, with ductile fracture phenomenon driven by Bauschinger plasticity non-linear mechanical processes, depending of the plastic strain [4].

While previous studies (e.g., Kuwamura and K. Yamamoto [5]) have identified this issue, models and mechanisms to characterize ULCF are not well established. Prediction models for the cyclic life of materials are thus often based on the alternating plastic and damage strain amplitude. The most commonly used relationship between the alternating damage and plastic strain and the life cycles is the so-called uniaxial Manson–Coffin law ([2], [6]), based on small uniaxial strains formulation. This law is essentially a two parameter power law curve and can be plotted in a log–log scale as a straight line where the slope of the curve depicts the exponent of the power law relationship.

The ULCF mechanical processes cannot be modelled using traditional fracture mechanics and fatigue models. Primarily, ULCF is often accompanied by large inelastic strain (damage and/or plasticity), which may invalidate stress intensity-based ΔK or ΔJ approaches [7]. Second, the induced loading histories are extremely random with very few cycles, making them difficult to adapt to conventional cycle counting techniques such as rain flow analysis ([8], [9]) or strain life approaches. Finally, ΔK or ΔJ methods, require an initial sharp crack or flaw, which is absent in many structural details. These limitations, coupled with the large strain advanced finite-element formulation methods, create the need for an improved understanding of the underlying ULCF process and the development of models to predict it.

Since 1950s, numerous experimental programs have been carried out to calibrate the material constants for different steels and a large amount of information is available . The experimental data is usually plotted on a log–log scale with the abscissa the number of life cycles and the coordinate the plastic strain amplitude, which is known as the $\Delta\varepsilon^p - N$ curve. From the experimental results, it is observed that the Manson–Coffin law does not fit well in the range of very low life cycles, i.e. about less than 100 cycles [3].

In this context, a new model for fatigue damage and plasticity assessment under ULCF is presented. ULCF damage is bounded by monotonic ductile failure and low-cycle fatigue (LCF). Typically, models for ULCF are extensions of LCF models. However, it is recognized in the literature that LCF models are not fully adequate without any kind of correction.

Therefore, the proposal presented in Martinez et al. [10] and in the current paper presents a new focus for the ULCF modelling. The complete nonlinear constitutive model is an extension of a given plasticity model to incorporate the damage effects due to cyclic action. It is an energetic based approach that accounts for the energy dissipated during the plastic action and compares it with a fracture energy that has to be calibrated by experiments. This is a coupled approach where damage due to cyclic action impacts directly on the stress-strain response.

The present work is centered on the large scale validation of the nonlinear constitutive model for cyclic and monotonic loading conditions. The model is the well-known Barcelona plastic damage model, proposed by Lubliner et al. [11]. An innovative application is given to this formulation by considering it for the cyclic loading case and incorporating a Friederick-Armstrong kinematic hardening law that allows the description of phenomena like cyclic ratcheting (under stress control conditions) or cyclic stress relaxation (under strain control or elastically constrained conditions). A new isotropic hardening law is also developed especially for steel materials, designed to reproduce their hardening and softening performance under monotonic and cyclic loading conditions. The exact expression of the constitutive law and the thermodynamic formulation of the model are presented in Martinez et al. [10], [12] and Barbu et al. [13].

In Sections 2 and 3 a summary of the new isotropic hardening law is presented with emphasis on small improvements made with respect to the expressions presented in Martinez

et al. [10] . In Section 4 the complete calibration procedure on small scale samples is presented step by step. In Section 5 results are shown for straight pipes under monotonic combined loading: uniaxial displacement and internal pressure. Two different loading histories are taken into account that exhibit different failure modes. Section 6 illustrates the results made on a 16-inch 90° elbow subjected to a variable in-plane displacement and internal pressure. Finally, in Section 7 conclusions are drawn as to the large scale behavior obtained with the proposed nonlinear constitutive model.

2. ULCF constitutive model

This work will not describe the complete plastic damage model, as it can be obtained from [10] and [11].

The inelastic theory of plasticity can simulate the material behavior beyond the elastic range, taking into account the change in the strength of the material through the movement of the yield surface, isotropic and kinematic. It is assumed that each point of the solid follows a thermo-elasto-plastic constitutive law (stiffness hardening/softening) ([11], [14], [15] and [16]).

The yield surface is defined by a function *F* that accounts for the residual strength of the material, which depends on the current stress state, the temperature and the plastic internal variables. This *F* function has the following form, taking into account isotropic and kinematic plastic hardening (Bauschinger effect - Lemaitre and Chaboche [17]),

$$F(S_{ij},\gamma^p,\theta) = f(S_{ij}-\alpha_{ij}) - K(S_{ij},\kappa^p,\theta) \le 0 \qquad (1)$$

where $f(S_{ij}-\alpha_{ij})$ is the uniaxial equivalent stress functions depending of the current value of the stress tensor S_{ij}, α_{ij} is the kinematic hardening internal variable, $K(S_{ij},\kappa^p,\theta)$ is the plastic strength threshold, κ^p is the plastic isotropic hardening internal variable, and θ is the temperature at current time t ([10], [11], [14], [15] and [16]).

2.1 Kinematic Hardening

Kinematic hardening accounts for a translation of the yield function and allows the representation of the Bauschinger effect in the case of cyclic loading.

This translation is driven by the kinematic hardening internal variable α_{ij} which, in a general case, varies proportionally to the plastic strain of the material point [17]. There are several laws that define the evolution of this parameter. Current work uses a non-linear kinematic hardening law, which can be written as:

$$\dot{\alpha}_{ij} = c_k \dot{E}^P_{ij} - d_k \alpha_{ij} \dot{p} \qquad (2)$$

where c_k and d_k are material constants, $\dot{E}^P_{ij}$ is the plastic strain increment, and $\dot{p}$ is the increment of accumulative plastic strain, which can be computed as: $\dot{p} = \sqrt{2/3 \cdot \dot{E}^p_{ij} : \dot{E}^p_{kl}}$.

2.2 Isotropic Hardening

Isotropic hardening provides an expansion or a contraction of the yield surface. The expansion corresponds to hardening and the contraction to a softening behavior.

The evolution of isotropic hardening is controlled by the evolution of the plastic hardening function K, which is often defined by an internal variable κ^p. The rate equation for these two functions may be defined, respectively:

$$\begin{aligned} \dot{K} &= \dot{\lambda} \cdot H_k = h_k \cdot \dot{\kappa}^p \\ \dot{\kappa}^p &= \dot{\lambda} \cdot H_{\mathrm{k}} = \dot{\lambda} \cdot \left[h_{\mathrm{k}} : \frac{\partial G}{\partial S} \right] = h_{\mathrm{k}} \cdot \dot{E}^p \end{aligned} \tag{3}$$

where k denotes scalar and $\mathbf{k}$ states for a tensor function. Depending on the functions defined to characterize these two parameters different solid performances can be obtained.

3. New isotropic hardening law

In the Barcelona model defined in Lubliner et al. [11], the laws defined are driven by the fracture energy of the material. This work presents a new law, especially developed for steel materials, that has been designed to reproduce their hardening and softening performance under monotonic and cyclic loading conditions. This law also depends on the fracture energy of the material and is derived from the hardening softening law presented in [11] and [12].

3.1. Fracture Energy

Classical fracture mechanics defines the fracture energy of a material as the energy that has to be dissipated to open a fracture in a unitary area of the material. This energy is defined as:

$$G_f = \frac{W_f}{A_f} \tag{4}$$

where W_f is the energy dissipated by the fracture at the end of the process, and A_f is the area of the surface fractured. The total fracture energy dissipated, W_f, in the fracture process can be used to define a fracture energy by unit volume, g_f, required in a continuum mechanics formulation:

$$W_f = G_f \cdot A_f \equiv \int_{V_f} g_f \, dV \tag{5}$$

This last equation allows establishing the relation between the fracture energy defined as a material property, G_f, and the maximum energy per unit volume:

$$g_f = \frac{W_f}{V_f} = \frac{W_f}{A_f \cdot l_f} = \frac{G_f}{l_f} \tag{6}$$

Thus, the fracture energy per unit volume is obtained as the fracture energy of the material divided by the fracture length. This fracture length corresponds to the distance, perpendicular to the fracture area, in which this fracture propagates.

In a real section, this length tends to be infinitesimal. However, in a finite element simulation, in which continuum mechanics is applied to a discrete medium, this length corresponds to the smallest value in which the structure is discretized: the length represented by a gauss point.

Therefore, in order to have a finite element formulation consistent and mesh independent, it is necessary to define the hardening law in function of the fracture energy per unit volume ([11], [15]). This value is obtained from the fracture energy of the material, G_f, and the size of the finite element in which the structure is discretized.

3.2. Hardening Function and Hardening Internal Variable

The hardening function defines the stress of the material when it is in the non-linear range. There are many possible definitions that can be used to fulfil the rate equations for the plastic strength threshold (3).

Here the use of a function that describes the evolution of an equivalent uniaxial stress state is proposed, like the one shown in Figure 1.

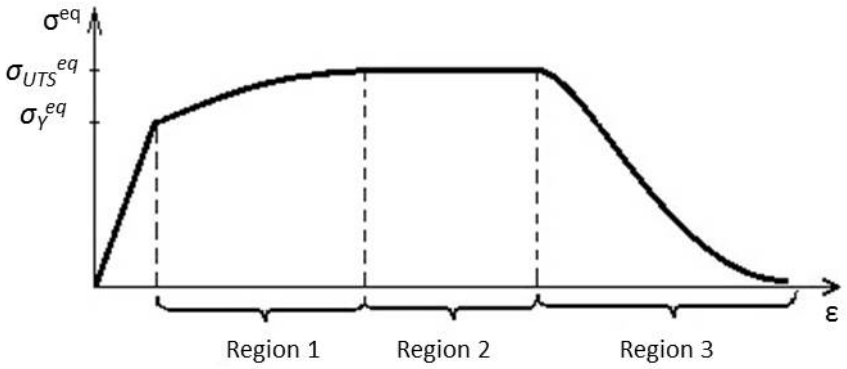

Figure 1. Evolution of the equivalent plastic stress

The equivalent stress state shown in Figure 1 has been defined to match the uniaxial stress evolution described by most metallic materials. This curve is different from the one presented in Martinez et al. [10] in the sense that the region obtained thru curve fitting is divided into two: a smaller region that is still dependent on curve fitting of experimental points and a linear region, with slope and extension defined by user. That helps ensure a fast integration of the stresses in the constitutive model by converging to the same numerical tolerance in less iterations. The first region is, therefore, defined by curve fitting from a given set of equivalent stress-equivalent strain points. The curve used to fit the points is a polynomial of any user given order, defined using the least squares method. The data given to define this region is expected to provide an increasing function, in order to obtain a good performance of the formulation when performing cyclic analysis.

The second region, as mentioned above, is defined as a linear curve. This region is incorporated to facilitate the convergence of the problem. If region 1 and 2 were to be simulated with just one polynomial, the difference in slope between the beginning of the curve and the end of it would make it very difficult to ensure that the slope of the polynomial is always positive so that the solution doesn't converge to a local minimum. Generally speaking, in the case of ULCF and LCF nearly 80% or more of the internal energy of the material is spent between regions 1 and 2.

The third region is defined with an exponential function to simulate softening. The function starts with a null slope that becomes negative as the equivalent plastic strains increase. The exact geometry of this last region depends on the fracture energy of the material.

The hardening internal variable, κ^p, accounts for the evolution of the plastic hardening function, K. In current formulation κ^p is defined as a normalized scalar parameter that takes into account the amount of volumetric fracture energy dissipated by the material in the actual strain-stress state. This is:

$$\kappa^p = \frac{1}{g_f}\int_{t=0}^{t} S : \dot{E}^p dt \tag{7}$$

Using the definition of the hardening internal variable defined in equation (7), it is possible to define the expression of the hardening function as:

$$K = S^{eq}(\kappa^p) \tag{8}$$

It can be easily proven that the hardening function and internal variable defined in equations (7) and (8) fulfil the rate equations (3). And the h_k and $h_{\mathbf{k}}$ functions defined in this expression become:

$$\begin{aligned} h_k &= \frac{\partial S^{eq}}{\partial \kappa^p} \\ h_{\mathrm{k}} &= \frac{S}{g_t} \end{aligned} \tag{9}$$

3.3. Expressions of the hardening function

In this section, the exact numerical expressions used to define the new hardening law are discussed. This law is an evolved version of the one presented in Martinez et al. [10]. The region described by curve fitting in the above reference has been divided into two different regions (Region 1 and Region 2 in Figure 1). This has been done in order to optimize the constitutive law for converging to the same tolerance in fewer iterations and making feasible the large scale simulations presented in this paper. The length of the curve fitting region has been limited to a user defined value and past this value of the plastic strain a linear curve has been defined with a user defined slope. (see Figure 1).

Region 1: Curve fitting with polynomial

The first region is characterized with a polynomial defined by curved fitting from a given experimental data. The exact mathematical definition for this region can be found in Martinez et al. [10]. Among the different available methods that can be used to define this polynomial, the use of the least squares method is proposed due to its simplicity, computational cost, and good performance.

Although the equivalent plastic stress should depend on the plastic internal variable κ^p, in a cyclic simulation with isotropic hardening this approach will produce hysteresis loops with increasing stress amplitude (for a fixed strain amplitude). For this reason, current formulation

calculates the equivalent plastic stress using the value of the equivalent plastic strain, which is calculated as:

$$E_{eq}^{p} = \frac{S : E^{p}}{f(S)} \tag{10}$$

with $f(S)$ defined by the yield surface used to simulate the material.

Finally, the derivative of the hardening function can be calculated with the following expression:

$$\frac{dS^{eq}}{d\kappa^{p}} = \frac{dS^{eq}}{dE^{p}} \cdot \frac{dE^{p}}{d\kappa^{p}} = g_t \cdot \frac{\sum_{i=1}^{N} (i-1) \cdot a_{i-1} \left(E^{p}\right)^{i-2}}{\sum_{i=1}^{N} a_{i-1} \left(E^{p}\right)^{i-1}} \tag{11}$$

Expression (11) is valid for values of κ^{p} that are comprehended between 0 and $\kappa_1^{p} = g_{t1}/g_t$.

Region 2: Linear curve

When the equivalent plastic strain, as calculated with equation (10), equals the value of equivalent plastic strain at which region 2 is to begin, $E_{eq}^{p} = E_2^{p}$, where E_2^{p} is user defined, the threshold function is obtained taking into account the following considerations:

- The initial equivalent stress value is defined by the equivalent stress reached at the end of the first region ($S_1^{eq}(E_1^{p}) = a_0 + \sum_{i=1}^{N} a_i \cdot \left(E_1^{p}\right)^{i}$).
- The slope of the function is user defined: $u = \frac{S_2^{eq} - S_1^{eq}}{E_2^{p} - E_1^{p}}$.
- The volumetric fracture energy dissipated in this region is $g_{t2} = (S_1^{eq} + S_2^{eq}) \cdot (E_2^{p} - E_1^{p}) \cdot 0.5$.

With these considerations in mind, the resulting equation that relates the equivalent stress with the plastic strain is:

$$S^{eq}(E^{p}) = S_1^{eq} + u \cdot (E^{p} - E_1^{p}) \tag{12}$$

The expression of the equivalent stress as a function of the hardening variable is obtained combining equation (12 and (7), obtaining:

$$S^{eq}(\kappa^{p}) = \sqrt{\left(S_1^{eq}\right)^2 + 2 \cdot u \cdot g_t \cdot (\kappa^{p} - \kappa_1^{p})} \tag{13}$$

Expression (13) is valid for values of κ^p that are comprehended between $\kappa_1^p = g_{t1}/g_t$ and $\kappa_2^p = (g_{t1} + g_{t2})/g_t$. The value of the upper limit of the internal variable shows that it is necessary define a value for the volumetric fracture energy of the material larger than $g_{t1} + g_{t2}$. If the value defined is lower, the material will not be able to reach its ultimate stress as this will imply having a fracture internal variable larger than 1.0.

Region 3: Exponential softening

When the plastic internal variable reaches the volumetric plastic energy available in the first two regions: $\kappa^p = \kappa_2^p$. At this point, isotropic hardening is defined by region three. Its function is obtained with the following parameters:

- The initial equivalent stress value is defined by the equivalent stress reached at the end of the second region (S_2^{eq}).
- The initial slope of the function is zero.
- The volumetric fracture energy dissipated in this region is the remaining energy in the material: $g_{t3} = g_t - g_{t1} - g_{t2}$

With these considerations in mind, the governing equations are the same as in Martinez et al. [10]. The constitutive law described in Sections 2 and 3 has been implemented in the in-house code PLCd [18]. The code was programmed to allow OpenMP parallelization, which greatly reduced the computational cost of the large scale FE simulations, and makes use of the load advancing strategy proposed in [19] and [20].

4. Material calibration

The material characteristics for the numerical simulations will be obtained by conducting a calibration analysis on small scale specimens. The hardening –softening law presented in section 3 requires of the following material parameters:

- $\varepsilon_p - \sigma_p$ points obtained from uniaxial monotonic tensile tests necessary for curve fitting. They are important for a correct representation of the tendency of the monotonic curve.
- Kinematic coefficients in accordance with the type of hardening chosen. They are important for the exact adjustment of the monotonic curve and for an accurate description of the hysteresis loop.
- Equivalent plastic deformation, ε_{p1}^{eq}, at which the linear region starts. This parameter is important both in the monotonic curve and in the overall cyclic behavior as it ensures a stable behavior throughout the fatigue life.
- Equivalent plastic deformation, ε_{p2}^{eq}, at which softening starts.
- Fracture energy G_f required in the monotonic curve for adjusting the slope of the softening behavior and in the cyclic behavior for correctly calibrating the fatigue life of the specimen. When the entire energy is spent the specimen is considered completely fractured.

In this paper two different materials have been calibrated: X52 and X60, corresponding to the large scale simulations analyzed. The step by step calibration process is presented for the X60 material. The calibration process of X52 can be seen in [10].

In order to exemplify the calibration process, a smooth X60 specimen was chosen from the experimental program ran by Pereira et al. [21]. This experimental program includes monotonic tests and cyclic tests in the LCF and in the ULCF regime. LCF tests have been conducted both

with a -1 and a 0 reversion factor, while all the ULCF tests have a reversion factor equal to 0. The geometric characteristics of the specimen are shown in Figure 2. This material will be posteriorly used for the large scale simulation of the bent pipe under cyclic loading.

The specimen was meshed into 3456 quadratic hexahedral elements with 20 nodes each and 27 integration points, adding to a total of 17165 mesh nodes.

The procedure for the correct calibration of the material starts from the determination of the elastic modulus and of the elastic limit. These two parameters are determined statistically from the force – displacement recordings of both the monotonic and the cyclic tests by monitoring where the linear relation is lost between them. For this simulation an elastic modulus of $E = 1.95 \times 10^{11} N/m^2$ and an elastic limit of $\sigma_y = 3.80 \times 10^8 N/m^2$ were chosen.

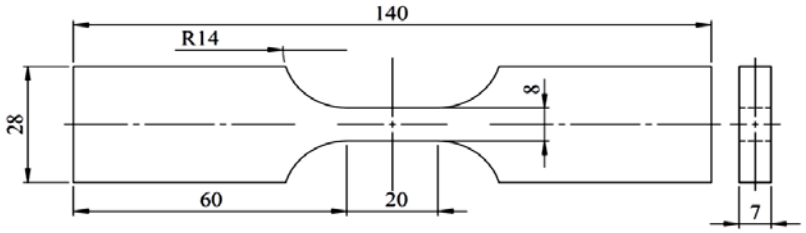

Figure 2. Geometry of the specimen used for calibration

The $\varepsilon_p - \sigma$ set of points chosen for this simulation are presented in Figure 3 as compared to the stress-strain curve of the small specimen chosen. At this point in the calibration procedure the series of chosen points have to follow the general tendency of the monotonic curve without reaching the same level of stress. The density of the points is recommended to be constant and quite high so that the polynomial interpolation can be effective. For this simulation the points were interpolated by a 5th order polynomial function.

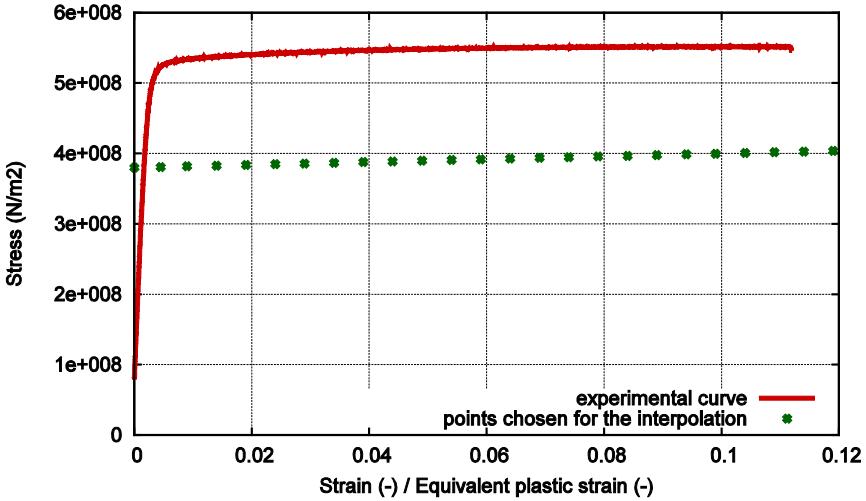

Figure 3. Comparison between the stress strain curve for the uniaxial monotonic tensile test and the points chosen for the numerical model

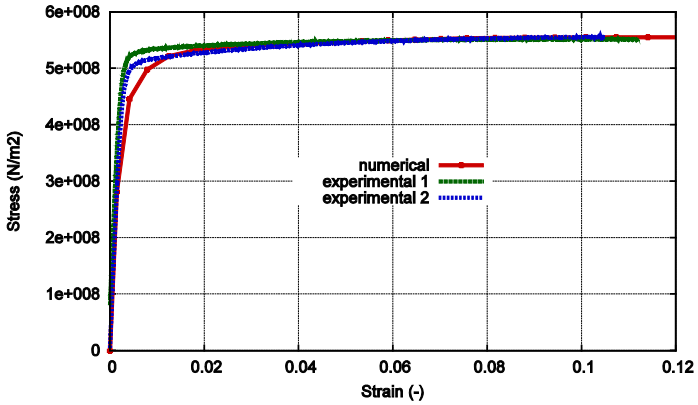

Figure 4. Monotonic stress- strain curve. Numerical vs. experimental.

The Armstrong- Frederick kinematic hardening function was used for this simulation. The kinematic coefficients chosen were $k_1 = 6 \times 10^{10}$ and $k_2 = 400$. In Figure 4 the effect of the kinematic hardening on the monotonic curve can be observed. In order to obtain this behavior a value of 0.1 was used for the ε_{p1}^{eq} parameter.

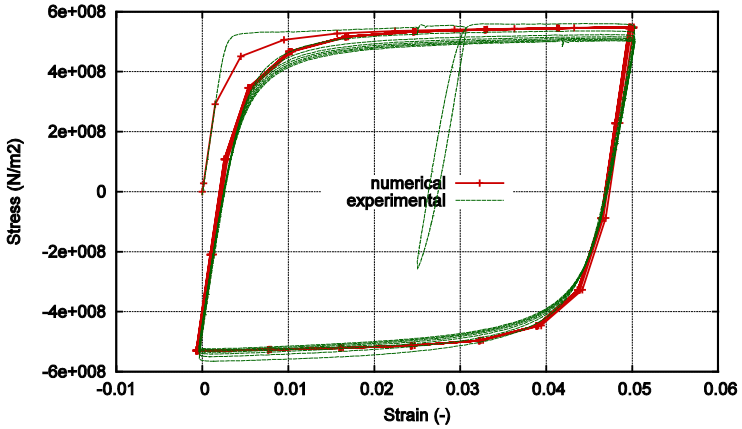

Figure 5. Stress-strain hysteresis loop for Δε=5%. Numerical vs. experimental.

It can be seen that taking into account the kinematic hardening causes the resulting stress-strain curve to elevate until it reaches the experimental monotonic ones. Also, the exact shape of the transition zone from linear to nonlinear is determined by the kinematic coefficients.

In Figure 5 the numerical hysteresis loop is compared to the experimental one for the Δε=5% case. In choosing the kinematic coefficients a compromise must be made between the accuracy of the monotonic behavior and of the cyclical one.

Once the kinematic coefficients have been established the next step in the calibration of the material is establishing the equivalent plastic deformation at which softening begins, ε_{p2}^{eq}, and the facture energy.

An experimental result has been chosen for the calibration, the Δε=5% case, that had an experimental fatigue life of 100 cycles. With a value of 13 for the ε_{p2}^{eq} and a fracture energy of 2.7 x 10^6 Nm/m^2 a total fatigue life of 100.35 cycles has been obtained from the numerical simulation. With these values, softening started in the 86th cycle, close to the end of the experimental life and a very low amount of energy was left for the softening branch so that it could be spent in a reduced number of cycles.

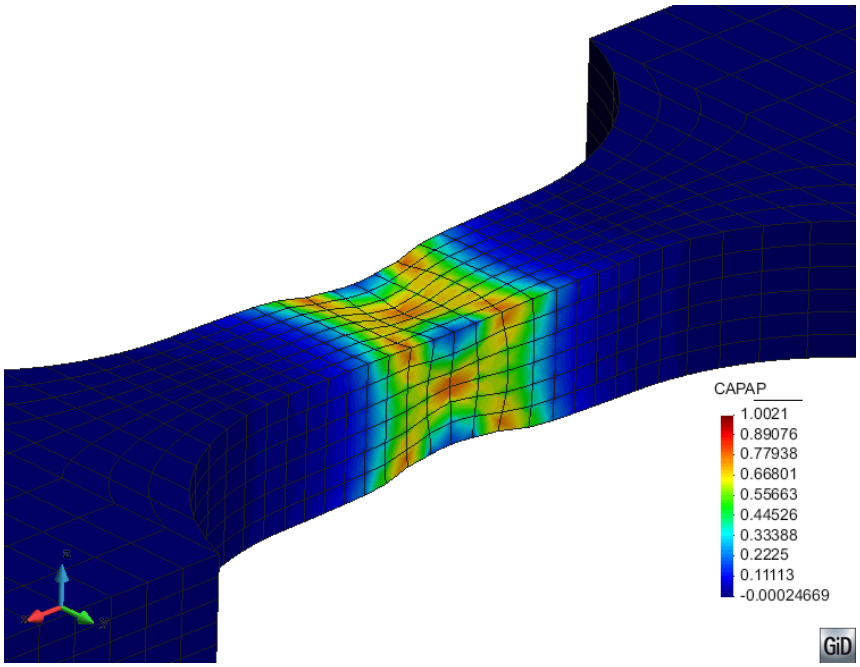

Figure 6. Distribution of the normalized plastic dissipation at total fracture

In Figure 6 the distribution of the plastic internal variable κ^p can be seen on the deformed shape of the specimen in the last step of the analysis for the calibration case. The null value for the plastic internal variable represents an elastic state in the material, while $\kappa^p = 1$ means the entire fracture energy of the material has been dissipated at that material point. It can be seen that the lateral necking is in accordance to standard metal fracture under uniaxial cyclic loading.

After the adjustment of the Δε=5% case, simulations were ran with the exact same material and with strain amplitudes of 2% and 8%. The results can be seen in Figure 7.

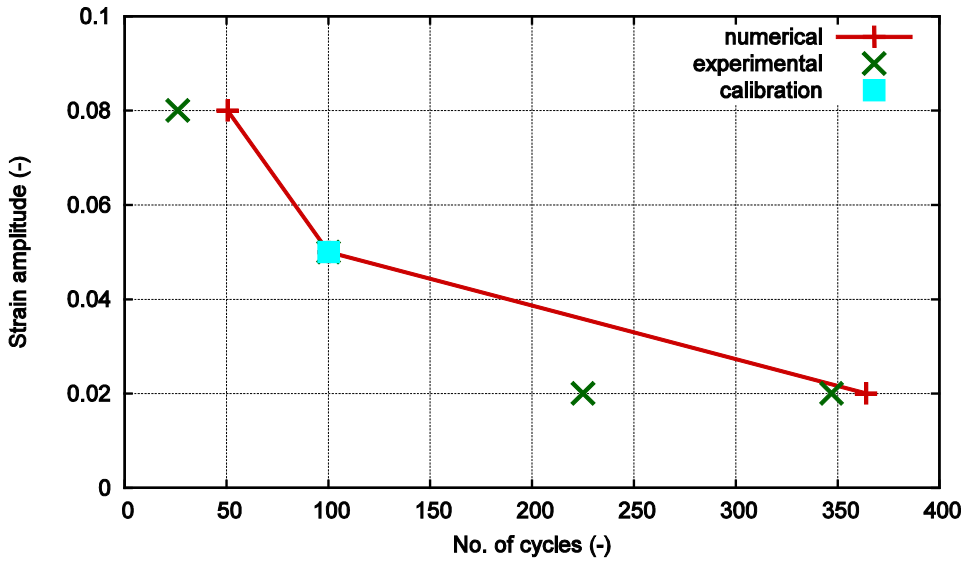

Figure 7. Comparison between numerical and experimental fatigue life for different strain amplitudes when calibrating with Δε=5%

In Table 1 and Table 2 a summary of the material properties as resulting from the calibration can be seen. A polynomial of the 5th degree was chosen for the curve fitting zone of the hardening function.

Coefficient no. 1	380000000,00
Coefficient no. 2	326947332,25
Coefficient no. 3	-861244568,93
Coefficient no. 4	1103673406,83
Coefficient no. 5	-657861660,66
Coefficient no. 6	147925577,48

Table 1. Polynomial coefficients for the X60 material as obtained from curve fitting

Young Modulus	$1.95 \cdot 10^5$	MPa
Poisson Modulus	0.30	
Elastic Stress (σ_Y^{eq})	380	MPa
Plastic Strain Limit for region 1(E_1^p)	10	%
Plastic Strain Softening (E_2^p)	1300	%
C1 kinematic hardening	$6.0 \cdot 10^4$	MPa
C2 kinematic hardening	400	
Fracture Energy	2.7	$MN \cdot m/m^2$

Table 2. Material parameters for the numerical model for an X60 steel

5. Large diameter straight pipe loaded monotonically

In order to analyze the capabilities of the constitutive model presented in previous sections, large scale numerical simulations of a straight pipe OD 168.3 x 4.78mm, X52 grade, will be conducted. The geometry of the model, boundary conditions and sequence of loading are established by the experiment made by Coppola et al. [22]. The specimen drawing can be seen in Figure 8.

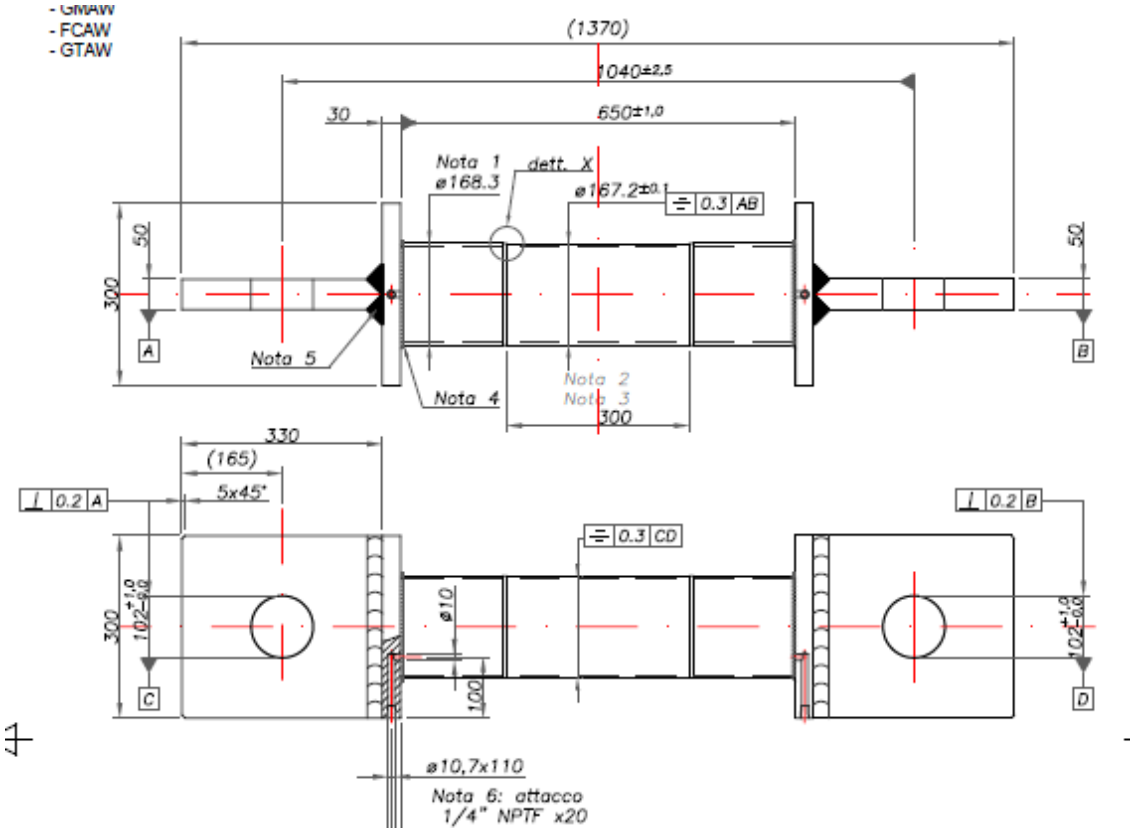

Figure 8. Specimen drawing for X52 full scale testing

5.1. Geometry of the model

The specimen consists of a straight pipe, with three differentiated sections. The central one is mechanized with a reduced thickness, as seen in Figure 9 and Table 3.

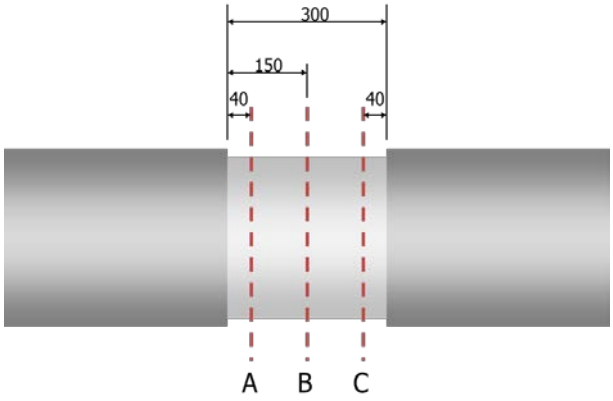

Figure 9. Sections of interest in the mechanization of the straight pipe

	Wall Thickness [mm]				Outer Diameter [mm]		
				OD 0°	164,2	163,88	164,04
Ref.	**sec 1: A**	**sec 2: B**	**sec 3: C**	**OD 45°**	168,3	168,5	168,42
0°	4,24	4,18	4,36	**OD 90°**	170,57	170,65	170,34
45°	3,85	4,19	3,99	**OD 135°**	166,89	166,64	166,04
90°	4,01	3,91	3,77				
135°	4,24	4,05	4,10	**WT Avg [mm]**	4,14	4,14	4,08

180°	4,16	4,17	4,16	**WT Min [mm]**	3,85	3,91	3,77
225°	4,15	4,19	4,13	**OD Avg [mm]**	167,49	167,42	167,21
270°	4,02	4,06	4,00	**ID Avg [mm]**	159,22	159,14	159,04
315°	4,41	4,37	4,16	**Aw [mm^2, WT Avg, OD Avg]**	2122,06	2123,62	2092,82
				Ki (WT Avg, OD Avg)	19,765	19,732	19,985

Table 3. Wall thickness and outer diameter at different points of each section of the pipe

In the numerical model the variation in thickness throughout the central zone has been accounted for, as well as the thickness variation throughout the same cross-section. Following, in Figure 10 a view of the mesh is shown. For this simulation quadratic hexahedral elements were used, each with 20 nodes and 27 integration points. The mesh consisted of 8162 elements and 45865 nodes.

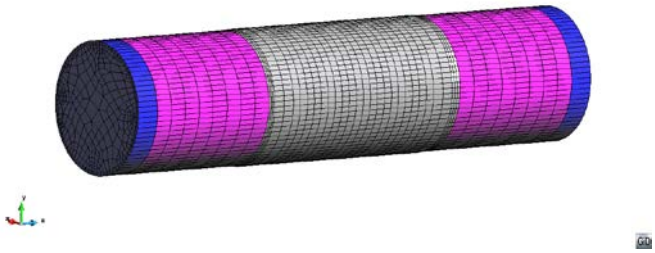

Figure 10. Mesh of hexahedral quadratic elements.

Regarding boundary conditions, one capped end of the pipe has its displacement restricted in all directions, while on the other capped end either force or displacement is applied as required by the loading history. When applying internal pressure, one end remains fixed while on the other one displacement in the longitudinal axis of the pipe is allowed (z-z axis in Figure 10) and restrained in the other two directions. The material of the mechanized part is an X52 steel. The outer parts have an elastic material, with the same Young modulus as X52. The pipe caps have been defined as a rigid material in agreement with the setup of the experiment (see Figure 8).

5.2. Loading history

For this simulation two load combinations were made. In the first case (SPEC1) a traction force was applied on one of the caps in the longitudinal pipe axis until a level of 400KN. Afterwards, an internal pressure was applied and gradually increased up to burst. Pipe failure occurred at 270bar with an associated total axial load of 940KN.

In the second case, the test has been done with internal pressure followed by tension. The internal pressure in the first step is 200 bars. Afterwards, the load was increased up to failure which occurred at 884KN mechanical load (1284KN total axial load). Pressure in the second step was maintained constant at 200 bars.

5.3. Material characteristics

The material parameters for the X52 steel have been obtained by undergoing the calibration process described in section 0 of this document. A polynomial of the 5th degree was chosen for the curve fitting zone of the hardening function. The polynomial coefficients as given by the least squares method are shown in Table 4.

The remaining material parameters are shown in Table 5.These material parameters were obtained by conducting a calibration process on small scale smooth sample specimens. The geometry of the samples and some calibration results for the cyclic case are presented in [10].

Coefficient no. 1	240000000,00
Coefficient no. 2	596993435,99
Coefficient no. 3	-1019807849,94
Coefficient no. 4	776714259,60
Coefficient no. 5	-265797084,38
Coefficient no. 6	33562252,72

Table 4. Polynomial coefficients for the X52 material as obtained from curve fitting

Young Modulus	$1.8 \cdot 10^5$	MPa
Poisson Modulus	0.30	
Elastic Stress (σ_Y^{eq})	240	MPa
Plastic Strain Limit for region 1(E_1^p)	15	%
Plastic Strain Softening (E_2^p)	50	%
C1 kinematic hardening	$6.0 \cdot 10^4$	MPa
C2 kinematic hardening	280	
Fracture Energy	0.4	$MN \cdot m/m^2$

Table 5. Material parameters for the numerical model for an X52 steel

In Figure 11, monotonic stress strain curve can be seen as obtained with the material parameters presented below. The comparison with the experimental monotonic curves for the X52 steel as obtained from Pereira et al. [21] can also be seen.

Figure 11 also exhibits the comparison between the numerical hysteresis loop shape and the experimental one. Although the straight pipe is loaded monotonically, when conducting the calibration analysis for the material, the shape of the hysteresis was one of the factors taken into account as the model is prepared to conduct monotonic and cyclic tests. The calibration process for a monotonic analysis follows the same guidelines as that of a cyclic analysis. The main difference resides in the plastic strain chosen as threshold for the softening behavior and in the fracture energy assigned to the material.

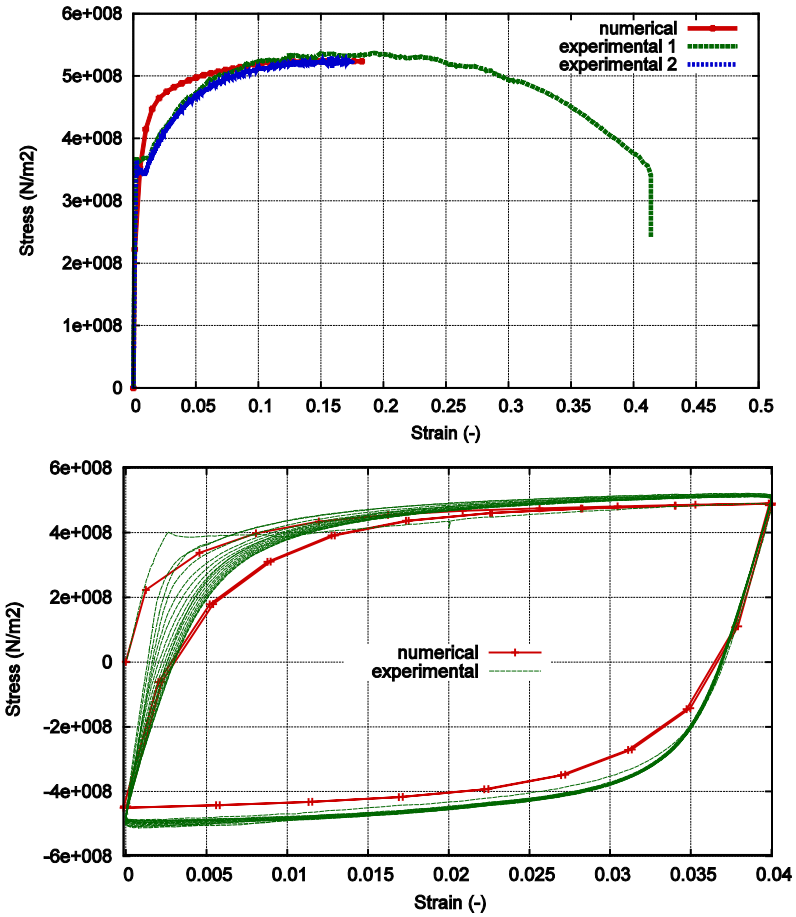

Figure 11. Stress-strain hysteresis loop for the monotonic case and for Δε=4%. Numerical vs. experimental.

5.4. Results and discussion

Case no. 1 - Tension followed by pressure

In Figure 12, the comparison between the experimental and the numerical force-pressure measurements can be seen. The total reaction recorded by the numerical simulation reached a level of 948KN in the last converged increment, corresponding to an applied internal pressure of 278.1bars.

For this increment, the deformed shape of the specimen is shown in Figure 13, where the distribution of the hardening internal variable κ^p can also be seen. This variable is of relevance in showing the level of dissipated energy at material point level and, in this sense, gives a measure of the level of degradation suffered. Consequently, for $\kappa^p = 0$ the material is in an elastic state, while for $\kappa^p = 1$ the material has reached total failure at that material point.

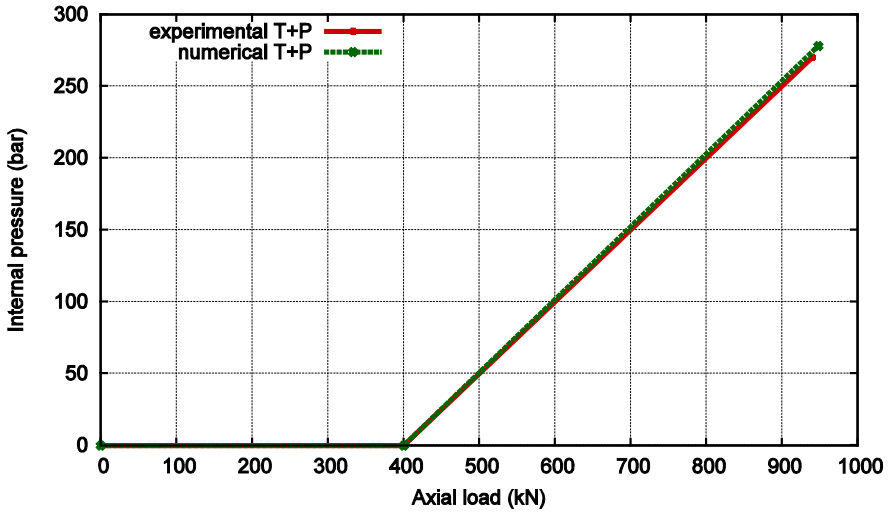

Figure 12. Comparison between the numerical and experimental results for the SPEC 1 case

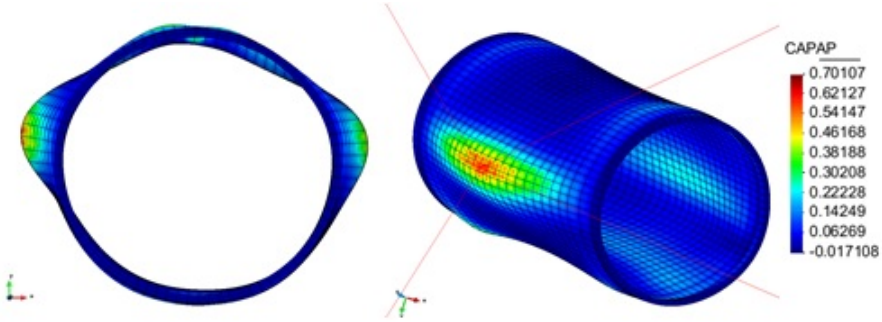

Figure 13. View of the deformed shape at the end of the analysis with an indication of the most damaged material point in the geometry

From the deformed shape it can be seen that the pipe failure is oriented following the direction of least resistance represented by the minimum thickness area. This is in agreement with the experimental localization of the failure as can be seen in Figure 14a.

Also, there is good agreement of the failure mode between the experiment and the numerical simulation with a final burst opening oriented in the longitudinal direction. In the numerical model the burst area is represented by the localized plastic strain accumulation reflected in the distribution of the normalized dissipation parameter.

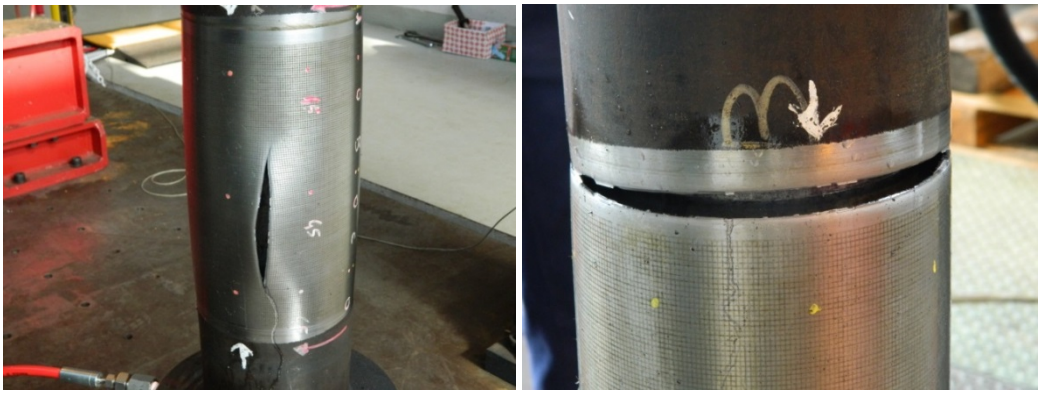

Figure 14. View of the pipe burst as recorded by the experiment for (a) the SPEC1 test and (b) SPEC2 test

Figure 15 shows the evolution of the hardening internal variable κ^p at the most damaged integration point in the material. Its exact location is indicated in Figure 13. As it can be seen from Figure 15, the simulation converged up until a maximum value of the κ^p internal variable of 0.7. Given that the internal pressure has been applied in constant increments of 2.7 bars per analysis step, it can be seen that the evolution of the κ^p parameter exhibits an exponential curve. Taking into account this tendency and extrapolating on the last converged increment that had a value of 0.7, loss of convergence seems to have occurred when the plastic internal variable reached a value very close to 1, corresponding to an open crack generated at the material points where the entire fracture energy of the material has been spent. However, this value is not visible in Figure 15 since convergence was not reached for this increment.

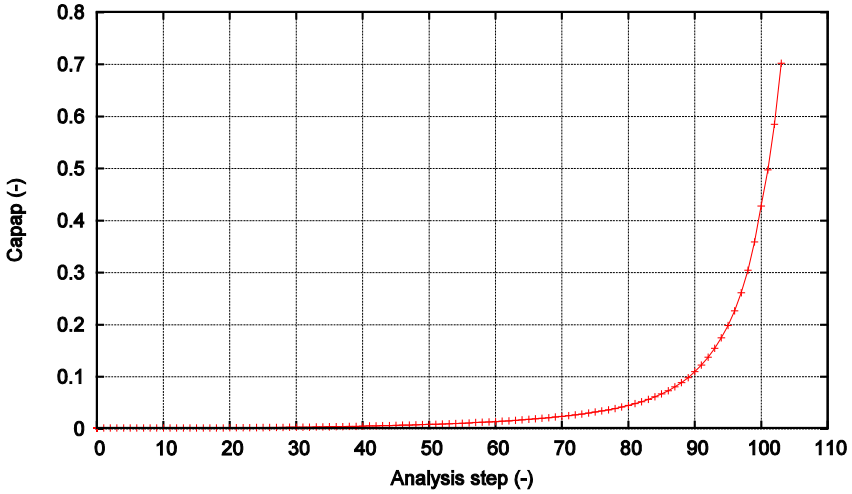

Figure 15. Evolution of the κ^p variable when applying internal pressure in constant steps of 2.7 bars

Case no. 2 – Internal pressure followed by tension

In Figure 16 the comparison between the experimental and the numerical force-pressure measurements can be seen for this case.

The total reaction recorded by the numerical simulation reached a level of 1167KN in the last converged step, corresponding to a total applied displacement of 1.375m. The experimental failure occurred at a total axial load level of 1284kN.

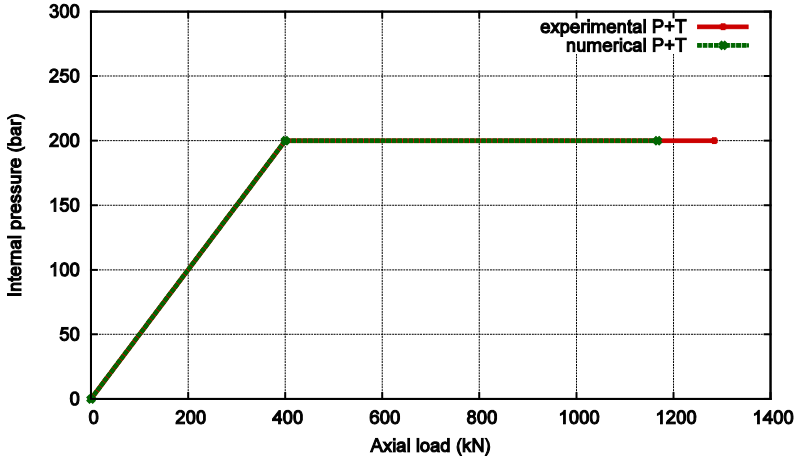

Figure 16. Comparison between the numerical and experimental results for the SPEC 2 case

As specified before, during the applied displacement stage the internal pressure was maintained constant at a level of 200 bars. For the last step of the simulation the deformed shape is shown in Figure 17, where the distribution of the hardening internal variable κ^p can also be seen.

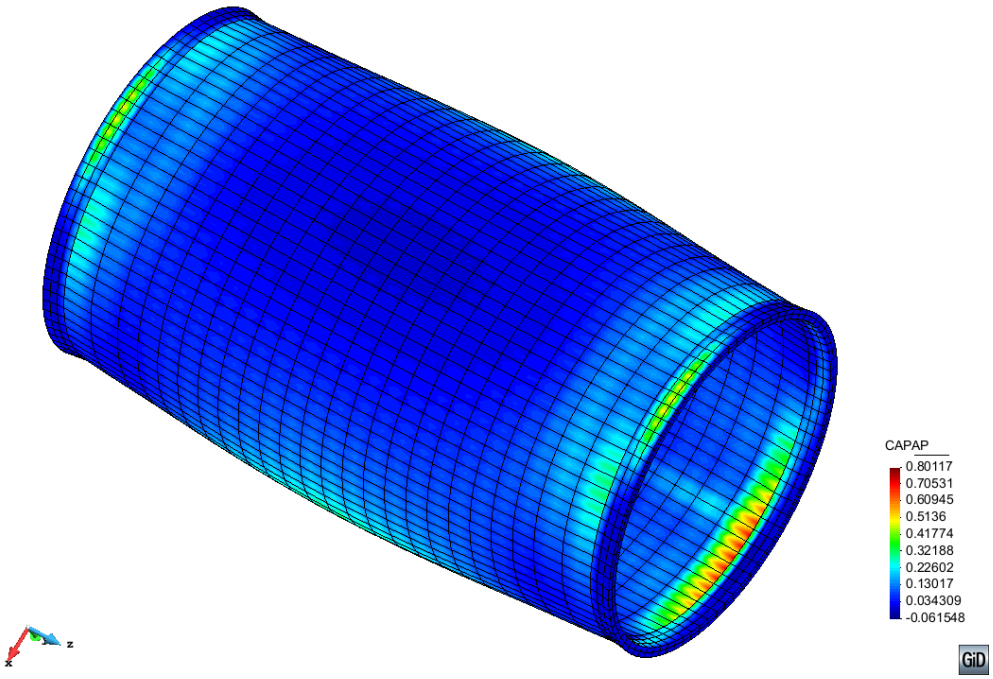

Figure 17. View of the deformed shape with an indication of the element where the maximum dissipation is recorded

The localization of the failure zone corresponds to the behavior shown in the experiment, presented in Figure 14b. When considering the pipe cross section where the maximum dissipation is present, the most stressed area is directed towards the smallest thickness in that particular circumference, corresponding with the data recorded by the experimental campaign and taking into account the orientation of the numerical model with respect to that of the experimental setting. The failure mode is a tensile one, in agreement to the applied sequence of loading.

6. Bent pipe under variable cyclic loading

6.1. Geometry of the model

Following the validation of the constitutive model made in Martinez et al. [10] on small scale specimens, the model is to be applied to large scale numerical simulations of a bent pipe. The geometry of the model, boundary conditions and the sequence of loading are in accordance to the experiment made by Schaffrath et al. [23].

The specimen consists of a bended middle section (elbow pipe) and a straight pipe section at each end of the elbow. The fillet radius of the elbow pipe is three times the pipe diameter (R=3 x D). For the length of both straight pipe sections a value of five times the diameter (L=5 x D) was used, whereby the influence of the load introduction can be neglected.

For the numerical model a specimen made of X60 steel has been chosen from the experimental program, with a diameter of 406.4 mm and a wall thickness of 9.5 mm. The pipe has an elbow angle of 90°.

In Figure 18 a view of the mesh is shown. For this simulation quadratic hexahedral elements were used, each with 20 nodes and 27 integration points. The mesh consisted of 42853 elements and 213415 nodes. Three elements were considered in the pipe thickness.

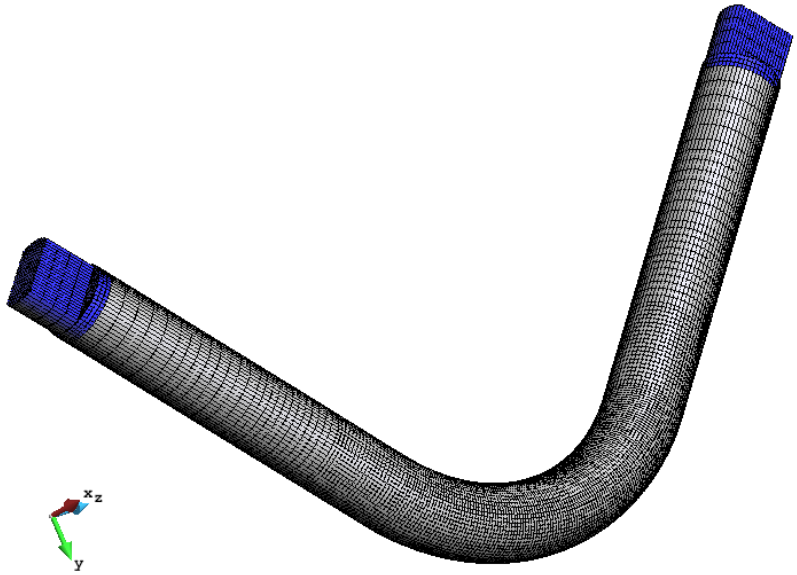

Figure 18. Mesh of hexahedral quadratic elements

6.2. Loading history

The loading history is based on the actual load history of the experimental test done by Schaffrath et al. [23]. The loading scheme was decided by the authors in accordance with the ECCS procedure ECCS-Nr. 45-1986 *Recommended Testing Procedure for Assessing the Behavior of Structural Steel Elements under Cyclic Loads* [24]. For practical reasons it was decided to neglect the mostly small difference between the compressive and tensile yield strain by choosing an average value $e_y = (e_y^+ + e_y^-)/2$ as the reference amplitude. In Table 6 the experimental loading sequence is described as a function of e_y.The value adopted for this parameter was set by [23] at ±82mm.

Step	Amplitude	Number of cycles
1	0.25 e_y	1
2	0.50 e_y	1
3	0.75 e_y	1
4	1.00 e_y	1
5	1.50 e_y	3
6	2.00 e_y	3
7	2.50 e_y	3
8	3.00 e_y	3
9	3.50 e_y	3
10	4.00 e_y	3
11	4.40 e_y	27

Table 6. Loading sequence for SP2 specimen

The entire loading sequence is comprised of 49 cycles with increasing amplitude, 44 of which have amplitudes in the plastic range. The reversion factor of the applied displacement is -1. The pipe is also submitted to internal pressure. First, the pipe is loaded until a level of internal pressure equal to 20 bars. Afterwards, it is submitted to the varying cyclic displacement presented in Table 5. The experimental test has shown that the internal pressure also oscillates when the cyclic displacement is applied.

The boundary conditions of the model were chosen in accordance with the setting of the experiment. One end of the model as presented in Figure 18 has its displacement blocked in the x, y and z direction while in the other end the cyclic displacement is applied in the z in-plane direction.

In the numerical simulation the loads have been applied in two stages. First, the internal pressure was applied and, in this stage, one end of the pipe was clamped and on the other end the pipe was only allowed in-plane gliding. The variable displacement was applied in the second stage on the deformed geometry obtained from applying the internal pressure. The movement was restrained in the two directions perpendicular to the in-plane one.

6.3. Material characteristics

The exact calibration procedure for the X60 material can be seen in Section 4, as well as the properties defined, that are presented in Table 1 and Table 2.

6.4. Results and discussion

In Figure 19 the comparison between the experimental force- displacement curve and the numerical one can be seen. The numerical curve is in very good agreement with the experimental one taking into consideration that the material calibration was done on small scale specimens with different experimental results.

It can be seen how in compression the constitutive equation tends to underestimate the maximum force level, while in traction the opposite tendency is present. Furthermore, this tendency is more obvious as the displacement increases. This is due to the existence of oscillations of the internal pressure applied in the experiment, caused by applying the cyclic

displacement. This oscillation of the internal pressure has not been taken into account in the numerical simulation.

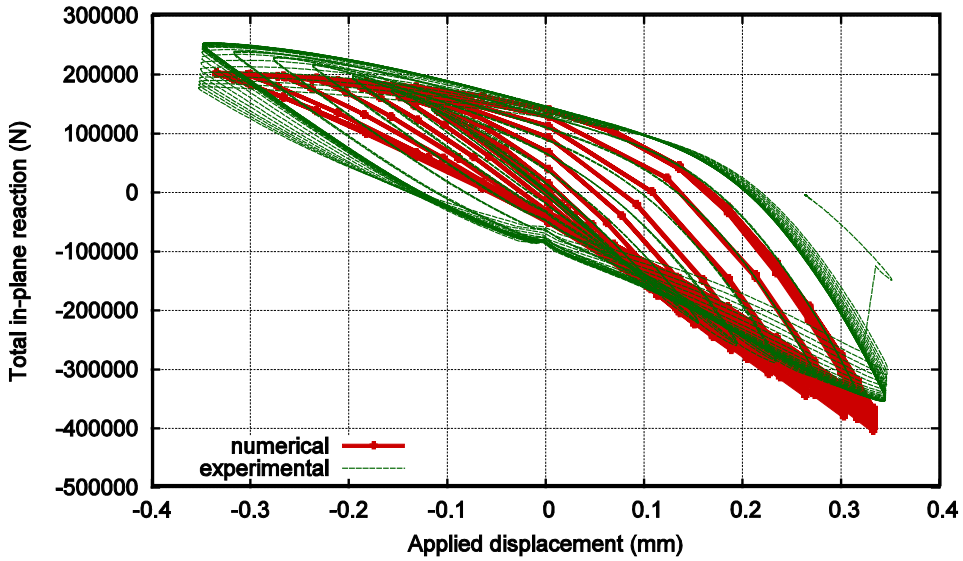

Figure 19. Force-displacement curve. Experimental vs. numerical

Regarding the fatigue life, the simulation lasted a total of 41.75 plastic cycles as compared to the experimental life of 44 complete cycles. This result also shows a good agreement between the experiment and the numerical simulation.

Figure 20 illustrates the deformed shape of the geometry in the last step of the analysis and presents the distribution of the plastic internal variable of the model. The deformed shape is represented with a scale factor of 2 in order to better reflect the general tendency. Only the central zone of the elbow is shown, as this is the zone where nonlinear effects appear. It can be seen that the failure mode resulting from the numerical simulation is by cross-sectional ovalization with a crack opening in the longitudinal direction of the elbow, at its flank. In Figure 21 the total strain distribution can be seen in the last step of the analysis in the three model axes. The distribution is also plotted on the deformed shape of the model, where the cross-sectional ovalization is clearly visible.

It can be seen that strain accumulation occurs in all three directions in the critical area where the normalized dissipation parameter, κ^p, accumulates.

The comparison of the failure mode obtained with the numerical simulation with the failure mode obtained in the experimental test (Figure 22) shows that the model has been able to capture the number of cycles to failure but has not been able to capture the failure mode shown in the experiment.

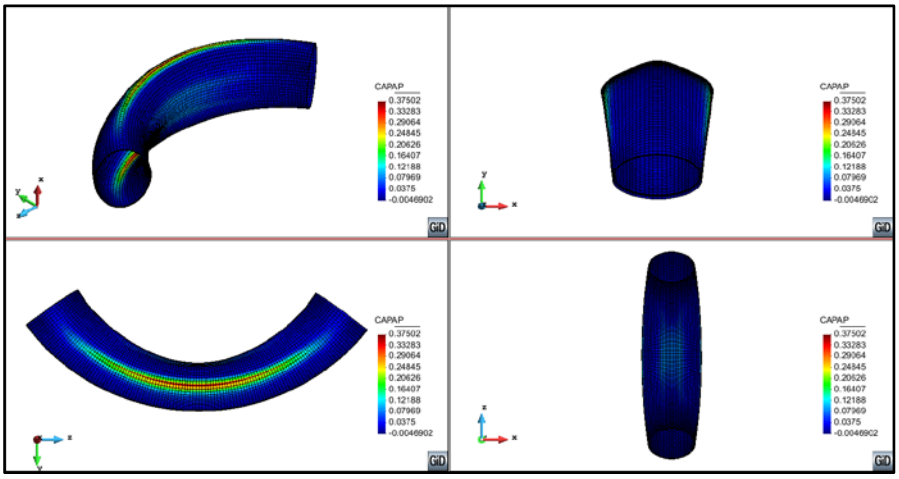

Figure 20. Distribution of the plastic internal variable of the model on the deformed shape (x2)

Under extreme loading conditions, such as the high repeated incursions in the nonlinear zone that the imposed displacement in this case causes, elbows exhibit two different failure modes. These are either significant cross-sectional ovalization or local buckling, as reported by the experimental work described in Sobel and Newman [25], [26], Dhalla [27] and Greenstreet [28], Tan et al. [29], Shalaby and Younan [30] and Suzuki and Nasu [31] for monotonic bending moments and Yahiaoui et al. [32], Slagis [33] and Fujiwaka et al. [34] for cyclic loading, and from the work of Karamanos et al. [35], [36], Pappa et al. [37], Varelis et al. [38], [39].

An important conclusion can be drawn from the work above mentioned. The first failure mode can be generally found when the elbow internal pressure is relatively low compared to the yield pressure, as is the case in the numerical simulation presented above.

The second failure mode, occurring due to local buckling is habitual in the cases where internal pressure is significantly higher. This is the failure mode yielded by the experiment made by Schaffrath et al. [23] as it can be seen in Figure 22.

For the case considered, the internal pressure applied to the elbow is 20 bars, which leads to a stress value, according to Barlow's formula: $\sigma = pD/2t = 42.77Mpa$. This is less than 10% of the yield strength for an X60 steel and, consequently, the pressure applied is less than 10% of the internal yield pressure. This puts us in the first yield mode, according to previous results found in literature. The failure due to local buckling obtained for a low value of the internal pressure by Schaffrath et al. [23] can, however, be a consequence of residual stresses generated in the bending process of the pipe combined with local defects that favored the formation of the buckle in the area shown by the experiment.

Summarizing, the number of cycles the simulation lasted and the force displacement curve are in good accordance between the numerical model and the experiment and the numerical failure mode is different from the experimental one but justifiable given the low internal pressure.

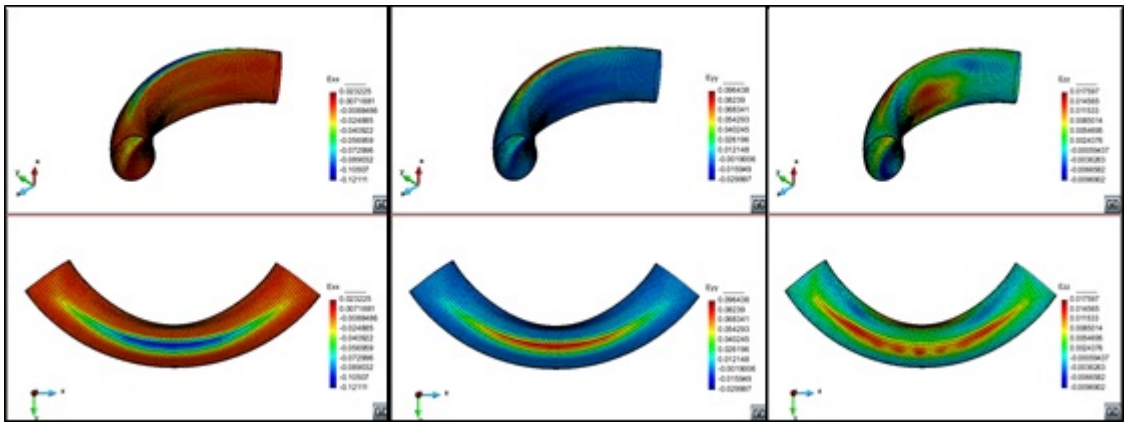

Figure 21. Distribution of the total strain in the three model axes on the deformed shape of the model (x2)

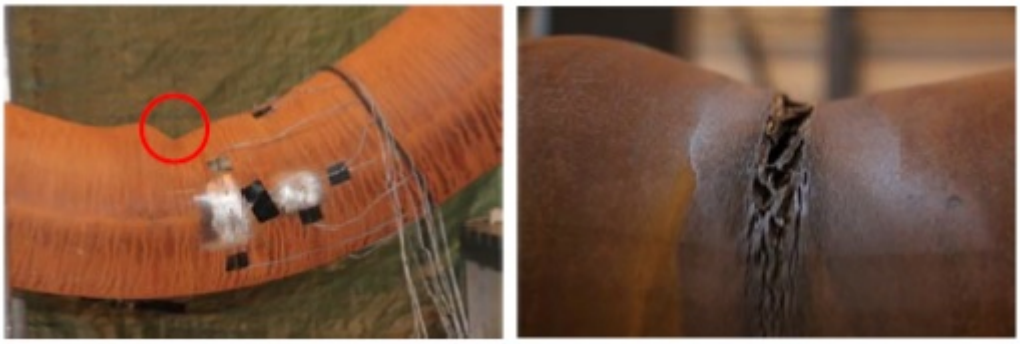

Figure 22. Experimental failure (Schaffrath et al. [23])

In order to assess the capability of the constitutive model to represent both failure modes, a different numerical simulation was done where the internal pressure applied was increased to 220 bars, in order to approximately reach the yield stress. Afterwards, the elbow was subjected to a monotonically increasing in-plane closing displacement.

The model used for this simulation is shown in Figure 23. Given the fact that this problem is highly nonlinear and the failure mode expected is achieved thru a local instability (local buckle), in order to achieve convergence when applying the displacement, an initial buckle was imposed on the model. This ensures that, when the internal pressure is sufficiently high, the plastic strain accumulation is directed toward this zone thus enabling model convergence.

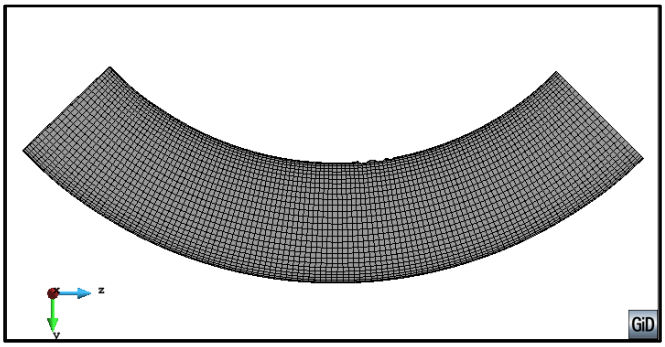

Figure 23. Geometry of the model with the initially imposed buckle

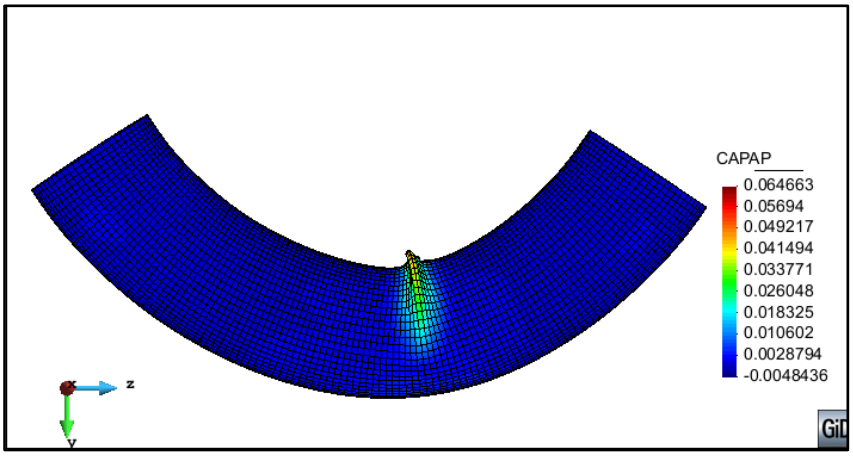

Figure 24. Distribution of the plastic internal variable of the model on the deformed shape

The final applied closing displacement up until which the problem converged was 2.69m, nearly 65% of the total in-plane geometry opening. In Figure 24 the distribution of the plastic internal variable is shown in the last converged analysis step on the deformed shape of the model with a scale factor of 1, and, as expected, it exhibits a concentration in the imposed buckle zone.

The purpose of this second simulation was to assess the capability of the numerical formulation to illustrate both failure modes in accordance to the level of internal pressure applied.

From the above numerical simulations it is clear that the failure mode obtained with the formulation is highly dependent on the level of internal pressure applied. A series of six monotonic simulations have been run varying the internal pressure applied initially and applying afterward an in-plane closing displacement. The maximum dissipation zone was assessed when the applied displacement reached the maximum one imposed in the cyclic large scale initial experiment (see Table 6).

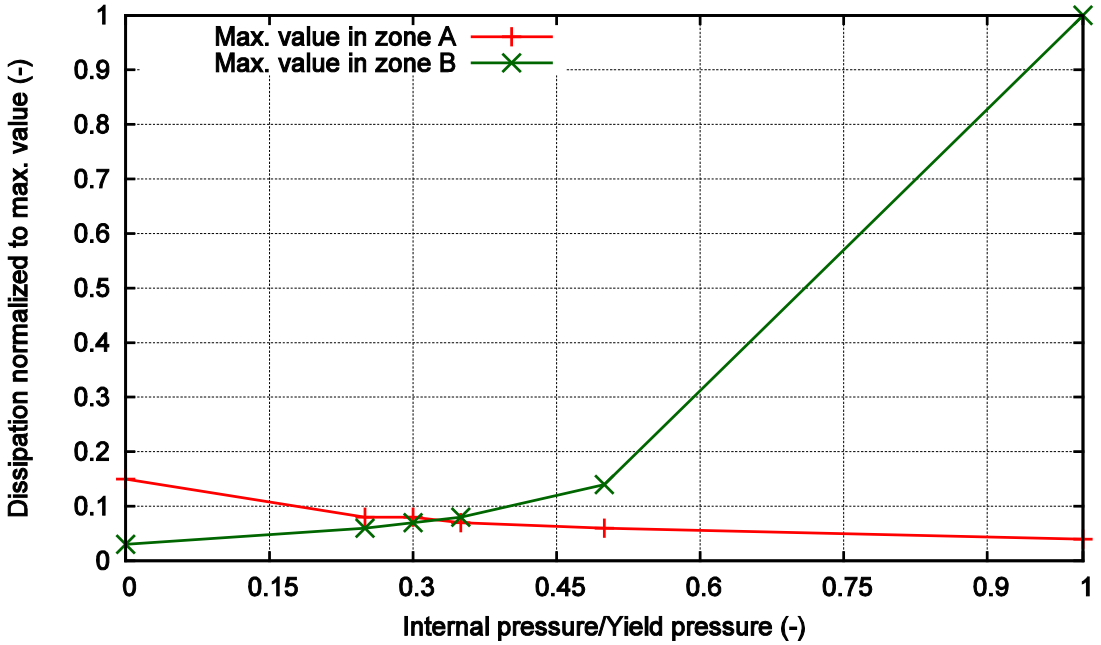

Figure 25. Evolution of the maximum dissipation in the two areas of interest

In Figure 25 the evolution of the maximum dissipation in the geometry is presented in the two areas that are specific to each failure mode: elbow flanks for the ovalization mode (zone A in Table 7 and Figure 25) and internal elbow curvature for the local buckling (zone B in Table 7 and Figure 25).

Py (%)	Zone A	Zone B
0	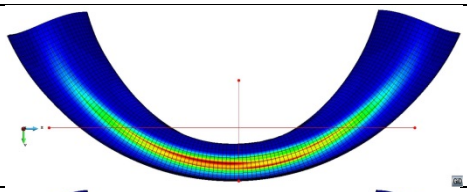	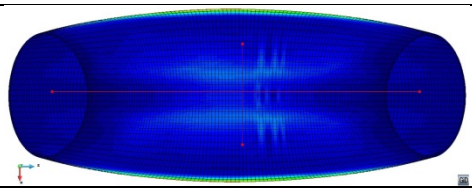
30	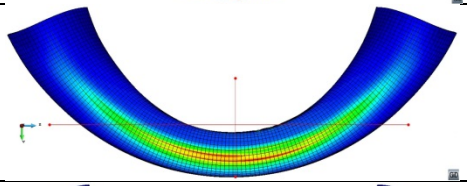	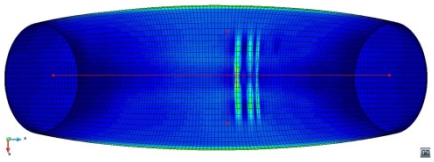
35	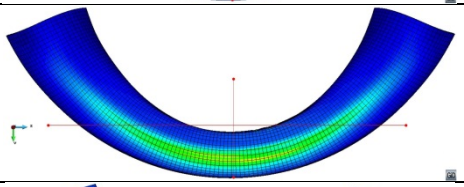	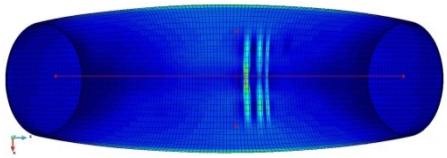
100	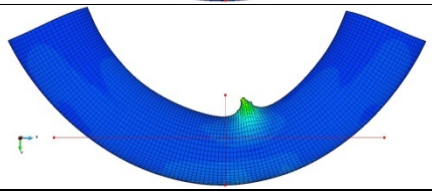	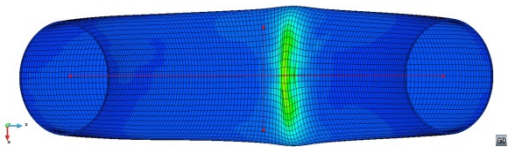

Table 7. Distribution of the maximum dissipation normalized to the fracture energy on the deformed shape of the model (x5).

From both Table 7 and Figure 25 it can be seen that the switch from the ovalization failure mode to the local buckling occurs between 30 and 35% of the yield internal pressure, since for the 30% case the maximum dissipation is recorded in the elbow flanks and for the 35% case it is present in the buckled area.

7. Conclusions

After validating the new constitutive law, especially formulated for the monotonic and cyclic behavior of steel, on small scale specimens, large scale simulations have been conducted to assess its capabilities. Even though the law has been designed for the particular case of cyclic loading, its behavior was also assessed on a straight pipe loaded monotonically. The results are very promising, with an error of 0.8% in the total axial load at failure for the first case where tension followed by internal pressure was applied. For the second case, internal pressure followed by tension until failure, the error was higher in terms of total axial load, of 9.11%, still below a 10% threshold.

Regarding the ULCF in-plane bending simulations conducted on a 16-inch 90° elbow, the results were in good agreement with the experimental test in terms of force-displacement hysteresis loops and total fatigue life of the specimen, where the error in life prediction was of 5.11% on the safety side for the numerical simulation.

The failure mode obtained by means of the numerical simulation was in agreement to the one found in literature for low internal pressure, but not in agreement with the particular experimental test used for comparison. An analysis of the dependence of the failure mode to the internal pressure applied has been conducted and the limit internal pressure between the two modes has been determined, showing that the formulation is capable of obtaining both failure types.

Finally, it should be remarked that the material calibration for both experimental tests reproduced (straight pipe and elbow) has been performed using data from other experimental tests (small samples). This proves the excellent prediction capabilities of the formulation, as it has been able to reproduce accurately the force-displacement response, the maximum load applied and the failure mode in both loading patterns: monotonic and cyclic.

Acknowledgements: This work has been supported by the Research Fund for Coal and Steel through the ULCF project (RFSR-CT-2011-00029), by the European Research Council under the Advanced Grant: ERC-2012-AdG 320815 COMP-DES-MAT "Advanced tools for computational design of engineering materials", by the research collaboration agreement established between Abengoa Research and CIMNE and by the Spanish Government program FPU: AP2010-5593.

REFERENCES

[1] Yao, J. T. P. and Munse, W. H. ,1961. Low-cycle fatigue of metals–literature review. Serial no. SSC-137, first progress report of project SR-149 to the ship structure committee on low-cycle fatigue of metals - literature review.

[2] Coffin, L. F., 1962. Low cycle fatigue-a review. Appl Mater Res 1962; 1(3): 129–41.

[3] Xue, L, 2008. A unified expression for low cycle fatigue and extremely low cycle fatigue and its implication for monotonic loading, Int. J. Fatigue, 30, 1691-1698

[4] Anderson, T. L., 1995. Fracture mechanics. 2nd Ed., CRC, Boca Raton, Fla.

[5] Kuwamura, H. and Yamamoto, K., 1997. Ductile crack as a trigger of brittle fracture in steel. J. Struct. Eng., 123 (6), 729–735.

[6] Manson, S.S., 1954. Behavior of materials under conditions of thermal stress. Technical Report NACA-TR-1170, National Advisory Committee for Aeronautics. Report 1170.

[7] Paris, P., Erdogan, F., 1963. A Critical Analysis of Crack Propagation Laws – ASME, J. Basic Engrg.; Vol.85: 528-534

[8] Miner, M., 1945. Cumulative damage fatigue- J. App. Mech; Vol. 12, pp. 159-164.

[9] Tatsuo, E., Koichi, M., Kiyohumi, T., Kakuichi, K. and Masanori M., 1974. Damage evaluation of metals for random of varying loading -Three aspects of rain flow method. Mechanical behavior of materials, Symp. Proc., Soc. Materials Scientists, Kyoto, Japan, Aug. 21–24

[10] Martinez, X., Oller, S., Barbu, L., Barbat, A. and De Jesus, A.M.P., 2015. Analysis of ultra-low cycle fatigue problems with the Barcelona plastic damage model and a new isotropic hardening law, Int. J. Fatigue , 73, pp 132-142

[11] Lubliner, J., Oliver, J., Oller, S. and Oñate, E., 1989. A plastic-damage model for concrete. Int. J. Solids Structures , 25(3): 299-326

[12] Martinez, X., Oller, S., Barbu, L. and Barbat, A., 2013. Analysis of ultra-low cycle fatigue problems with the Barcelona plastic damage model, Computational Plasticity XII. Fundamentals and Applications 352 – 363, ISBN 978-84-941531-5-0.

[13] Barbu, L.G., Oller, S., Martínez, X. and Barbat, A.H, 2014. Coupled plastic damage model for low and ultra-low cycle seismic fatigue. 11th World Congress on Computational Mechanics, p. 2955-2966, ISBN 978-84-942844-7-2.

[14] B. Luccioni, S. Oller and R. Danesi. Coupled plastic-damage model. Computer Methods in Applied Mechanics and Engineering, 129: 81-90 (1996)

[15] Oller, S., 2001. *Fractura mecánica. Un enfoque global*. Centre Internacional de Mètodes Numèrics a l'Enginyeria (CIMNE). Barcelona, Spain. ISBN: 84-89925-76-3

[16] S. Oller, O. Salomón, E. Oñate. A continuum mechanics model for mechanical fatigue analysis. Computational Materials Science (2005), 32(2): 175-195

[17] J. Lemaitre and J.-L. Chaboche. Mechanics of Solid Materials. Cambridge University Press. New York, USA, 1990

[18] PLCd Manual. Non-linear thermo-mechanic finite element code oriented to PhD student education. Code developed at CIMNE; 1991–to present. URL:<https://web.cimne.upc.edu/users/plcd/>.

[19] Barbu, L.G., Oller, S., Martinez, X. and Barbat, A. Stepwise advancing strategy for the simulation of fatigue problems, Computational Plasticity XII. Fundamentals and Applications (2013) 1153 – 1164, ISBN 978-84-941531-5-0.

[20] Barbu, L.G., Oller, S., Martinez, X. and Barbat, A. High cycle fatigue simulation: A new stepwise load-advancing strategy, Engineering Structures (2015) 97: 118-129, http://dx.doi.org/10.1016/j.engstruct.2015.04.012.

[21] Pereira, J.C.R., de Jesus, A.M.P., Xavier, J., Fernandes, A.A., Martins, B., , 2014. Comparison of the monotonic, low-cycle and ultra-low-cycle fatigue behaviors of the X52, X60 and X65 piping steel grades, Proceedings of the 2014 ASME Pressure Vessels & Piping Conference, ASME 2014 PVP, July 20-24, Anaheim, California, USA

[22] Coppola, T., Iob, F., Karamanos, S., Varelis, G., Schaffrath, S., Feldman, M., Thibaux, P., Large-scale monotonic and cyclic tests of pipeline components, Technical Report No: D4, Research Fund for Coal and Steel, RFSR-CT-2011-00029 (2013).

[23] Schaffrath, S., Novokshanov, D., Eichler, B., Münstermann, S., Characterization and simulation of X60 elbow pipes in case of ULCF loading , in 5th. European Conference on Computational Mechanics (ECCM V), 2014.

[24] ECCS Technical Committee 13, 1986. "Recommended testing procedures for assessing the behaviour of structural steel elements under cyclic loads", European Convention for Constructional Steelwork (ECCS), No 45

[25] Sobel, L. H., and Newman, S. Z., 1980, "Comparison of Experimental and Simplified Analytical Results for the In-Plane Plastic Bending and Buckling of an Elbow," ASME J. Pressure Vessel Technol., 102, pp. 400–409.

[26] Sobel, L. H., and Newman, S. Z., 1986, "Simplified, Detailed and Isochronous Analysis and Test Results for the In-Plane Elastic-Plastic and Creep Behaviour of an Elbow," ASME J. Pressure Vessel Technol., 108, pp. 297–304.

[27] Dhalla, A. K., 1987, "Collapse Characteristics of a Thin-Walled Elbow," ASME J. Pressure Vessel Technol., 109, pp. 394–401.

[28] Greenstreet, W. L., 1978, "Experimental Study of Plastic Responses of Pipe Elbows," Report No. ORNL/NUREG-24, Contract No. W-7405-eng-26.

[29] Tan, Y., Matzen, V. C., and Yu, L. X., 2002, "Correlation of Test and FEA Results for the Nonlinear Behavior of Straight Pipes and Elbows," ASME J. Pressure Vessel Technol., 124(4), pp. 465–475.

[30] Shalaby, M. A., and Younan, M. Y. A., 1998, "Limit Loads for Pipe Elbows With Internal Pressure Under In-Plane Closing Bending Moments," ASME J. Pressure Vessel Technol., 120(1), pp. 35–42.

[31] Suzuki, N. and Nasu, M., 1989. “Non-Linear Analysis of Welded Elbows Subjected to In-Plane bending”, Computers and Structures, 32, No.3/4, pp.871-881.

[32] Yahiaoui, K., Moffat, D.G., Moreton, D.N., 1996. “Response and cyclic strain accumulation of pressurized piping elbows under dynamic in-plane bending”, J. Strain Analysis for Engrg Design, 31 (2), pp. 135-151.

[33] Slagis, G.C., 1998 Experimental Data on Seismic Response of Piping Components, J. Pressure Vessel Technology, ASME, 120, pp.449-455.

[34] Fujiwaka, T. Rndou, R., Furukawa, S., Ono, S., Oketani, K., 1999. “Study on strength of piping components under elastic-plastic behavior due to seismic loading”, PVP Conference, Seismic engineering, PVP-Vol 137.

[35] Karamanos, S. A., Giakoumatos, E., and Gresnigt, A. M., 2003, “Nonlinear Response and Failure of Steel Elbows Under In-Plane Bending and Pressure,” ASME J. Pressure Vessel Technol., 125(4), pp. 393–402.

[36] Karamanos, S. A., Tsouvalas, D., and Gresnigt, A. M., 2006., “Ultimate Bending Capacity and Buckling of Pressurized 90 Deg Steel Elbows,” ASME J. Pressure Vessel Technol., 128(3), pp. 348–356.

[37] Pappa, P., Tsouvalas, D., Karamanos, S. A., and Houliara, S., 2008, “Ultimate Capacity of Pipe Bends Under Bending and Pressure,” Offshore Mechanics and Arctic Engineering Conference, Estoril, Portugal, ASME Paper No. OMAE2008-57358.

[38] Varelis, G. E., Karamanos, S. A., and Gresnigt, A. M., 2013, “Steel Elbow Response Under Strong Cyclic Loading,” ASME J. Pressure Vessel Technol., 135(1), p. 011207.

[39] Varelis, G. E., Ferino, J., Karamanos, S. A., Lucci, A., and Demofonti, G., 2013, “Experimental and Numerical Investigation of Pressurized Pipe Elbows Under Strong Cyclic Loading,” Pressure Vessel and Piping Conference, ASME, Paris, France, July 14–18, ASME Paper No. PVP2013-97977, p. V008T08A022.